

Ionic structure in liquids confined by dielectric interfaces

Yufei Jing, Vikram Jadhao, Jos W. Zwanikken, and Monica Olvera de la Cruz

Citation: *The Journal of Chemical Physics* **143**, 194508 (2015); doi: 10.1063/1.4935704

View online: <http://dx.doi.org/10.1063/1.4935704>

View Table of Contents: <http://scitation.aip.org/content/aip/journal/jcp/143/19?ver=pdfcov>

Published by the **AIP Publishing**

Articles you may be interested in

[Excluded volume effects in macromolecular forces and ion-interface interactions](#)

J. Chem. Phys. **136**, 074901 (2012); 10.1063/1.3684880

[Apparatus and method to measure dielectric properties \(\$\epsilon'\$ and \$\epsilon''\$ \) of ionic liquids](#)

Rev. Sci. Instrum. **80**, 044703 (2009); 10.1063/1.3117352

[Thermodynamics of ternary electrolytes: Enhanced adsorption of macroions as minority component to liquid interfaces](#)

J. Chem. Phys. **130**, 044502 (2009); 10.1063/1.3065071

[Electric conductivities of 1:1 electrolytes in liquid methanol along the liquid-vapor coexistence curve up to the critical temperature. III. Tetraalkylammonium bromides](#)

J. Chem. Phys. **122**, 104512 (2005); 10.1063/1.1866032

[Molecular dynamics simulations of simple dipolar liquids in spherical cavity: Effects of confinement on structural, dielectric, and dynamical properties](#)

J. Chem. Phys. **111**, 1223 (1999); 10.1063/1.479307



APL Photonics is pleased to announce
Benjamin Eggleton as its Editor-in-Chief



Ionic structure in liquids confined by dielectric interfaces

Yufei Jing,¹ Vikram Jadhao,^{1,a)} Jos W. Zwanikken,^{1,b)} and Monica Olvera de la Cruz^{2,c)}

¹Department of Materials Science and Engineering, Northwestern University, Evanston, Illinois 60208, USA

²Departments of Materials Science and Engineering, Chemistry, Chemical and Biological Engineering, and Physics and Astronomy, Northwestern University, Evanston, Illinois 60208, USA

(Received 14 May 2015; accepted 2 November 2015; published online 19 November 2015)

The behavior of ions in liquids confined between macromolecules determines the outcome of many nanoscale assembly processes in synthetic and biological materials such as colloidal dispersions, emulsions, hydrogels, DNA, cell membranes, and proteins. Theoretically, the macromolecule-liquid boundary is often modeled as a dielectric interface and an important quantity of interest is the ionic structure in a liquid confined between two such interfaces. The knowledge gleaned from the study of ionic structure in such models can be useful in several industrial applications, such as in the design of double-layer supercapacitors for energy storage and in the extraction of metal ions from wastewater. In this article, we compute the ionic structure in a model system of electrolyte confined by two planar dielectric interfaces using molecular dynamics simulations and liquid state theory. We explore the effects of high electrolyte concentrations, multivalent ions, dielectric contrasts, and external electric field on the ionic distributions. We observe the presence of non-monotonic ionic density profiles leading to a layered structure in the fluid which is attributed to the competition between electrostatic and steric (entropic) interactions. We find that thermal forces that arise from symmetry breaking at the interfaces can have a profound effect on the ionic structure and can oftentimes overwhelm the influence of the dielectric discontinuity. The combined effect of ionic correlations and inhomogeneous dielectric permittivity significantly changes the character of the effective interaction between the two interfaces. © 2015 AIP Publishing LLC. [<http://dx.doi.org/10.1063/1.4935704>]

I. INTRODUCTION

Many biological materials such as DNA and proteins as well as synthetic systems such as colloidal dispersions, polymeric gels, and emulsions are immersed in liquids that inhabit charged objects among which the most abundant are salt ions.^{1,2} In biology, the presence of these salt ions controls a wide variety of processes. For example, calcium ions play a key role in the pumping action of the heart and concentration gradients of sodium and potassium ions help to control nerve signaling.^{3,4} On the other hand, electrolyte ions help drive key processes involved in the generation and function of many synthetic materials such as the stabilization of colloidal dispersions and emulsions,^{5–7} morphological changes in hydrogels,⁸ and pattern formation in nanostructures.^{9,10}

Often, the macromaterials such as proteins or colloids themselves carry charge in which case the surrounding solution also contains counterions. Further, in some synthetic systems such as dielectric elastomers and supercapacitor devices, in addition to the charged macromaterial and counterions and salt ions, external electric fields are present. The structure of the ion-containing liquid near charged or

neutral materials determines how they assemble and interact and often modifies their functional properties. The knowledge of this so-called soft, ionic structure is exploited in designing double-layer supercapacitor for energy storage,^{11,12} stabilizing inks and paints, in water desalinization, and in the extraction of metal ions from wastewater.¹³ It is thus crucial to extract this soft, ionic structure associated with the fluid near a relatively rigid object such as a colloid or a biological macromolecule. Therefore, the computation of ionic structure has been the focus of recent experiments and theoretical studies.^{11,14–21}

Theoretically, the real system of macromolecules in an ion-containing liquid is often modeled in the following approximate way. The first approximation is to treat both the macromolecules and the surrounding liquid (solvent) as continuous media, thus removing the discrete character associated with their constituents. To account for the polarizabilities of the macromolecules (say a colloid, protein, or oil droplet) and the surrounding solvent (often water), the continuous medium is characterized with a dielectric constant, which often leads to a model system where the permittivity is only piecewise-uniform due to the differences in the dielectric permittivities of the macromolecules ($\epsilon \sim 2$ –10) and the surrounding solvent ($\epsilon \sim 80$). In the case when the density of macromolecules is high, the ionic structure is deformed as a result of the enhanced proximity of the macromolecules. In this scenario, the appropriate model to study involves an ion-containing liquid confined between two interfaces which represent the boundaries between macromolecule and the liquid medium.

^{a)}Present address: Department of Physics and Astronomy, Johns Hopkins University, Baltimore, Maryland 21218, USA. Electronic mail: vjadhao1@jhu.edu

^{b)}Present address: Department of Physics and Applied Physics, University of Massachusetts, Lowell, Massachusetts 01854, USA. Electronic mail: johannes_zwanikken@uml.edu

^{c)}Electronic mail: m-olvera@northwestern.edu

The small distance between the interfaces leads to the competition between inter-ionic electrostatic interactions and hard-core or steric interactions between the ions and the interfaces and between the ions themselves. Considering the difference in sizes between the macromolecules and the associated ions, it often suffices to treat the interfaces as planar. Also, owing to the narrowness of the gap between the interfaces, it becomes imperative to take into account the finite-size of the ions in the theoretical investigation. This model of ions of a finite, fixed diameter moving in a continuum solvent confined between two planar dielectric interfaces is useful in analyzing several properties of the aforementioned biological and synthetic materials and has been employed in several recent studies.^{14,18,22,23} Working with this model approximation, a quantity of interest is the ionic distribution (which encodes the structural information) within the confined liquid for various electrolyte concentrations, stoichiometric ratios, ion sizes, interfacial dielectric contrasts, gap between the interfaces, and presence of external electric field. Another important investigation is the study of how this soft ionic structure arrives at its equilibrium conformation and how it evolves dynamically in response to a change in external parameters such as pH, temperature, or tuning of the electric field or dielectric contrast.

The presence of multiple interfaces and associated dielectric heterogeneities and the necessity to suspend the assumption of point-size ions often complicate computing the desired ionic distributions. On the simulation side, while incorporating the finite size of the ions is relatively straightforward, treating the inhomogeneous dielectric response amounts to explicitly solving the Poisson equation at every step of the simulation in order to propagate the ionic degrees of freedom, which leads to very high computational costs. On the analytical side, while including the spatially dependent permittivity function is relatively straightforward, taking into consideration the correlations between the ions presents serious challenges and computational costs raised by the evaluation of the required anisotropic pair-correlation functions. Due to these difficulties, many simulation studies of ionic structure near interfaces assume dielectric homogeneity and theoretical approaches that go beyond mean field or Poisson-Boltzmann theory often retain the assumption of a structureless fluid of ions, with strong coupling corrections limited to a thin boundary layer. At the same time, recent research efforts have also focused on alleviating these problems and accurately extracting the ionic structure by developing sophisticated simulation procedures^{17,21,24–29} and advanced theoretical methods.^{14,18,30–36}

In this article, we carry out a systematic study of ionic structure in an electrolyte solution confined by two planar dielectric interfaces (see Fig. 1) using molecular-dynamics-(MD) based simulations and liquid state theory. We study the effects of the competition between electrostatic and steric interactions by evaluating the profiles for different ion concentrations. We evaluate the role of ion correlations^{37–41} in determining the ionic structure by considering electrolytes with different stoichiometric ratios (1:1, 2:1, 3:1). We also investigate in detail the role of dielectric mismatch at the interface by considering a variety of values for the

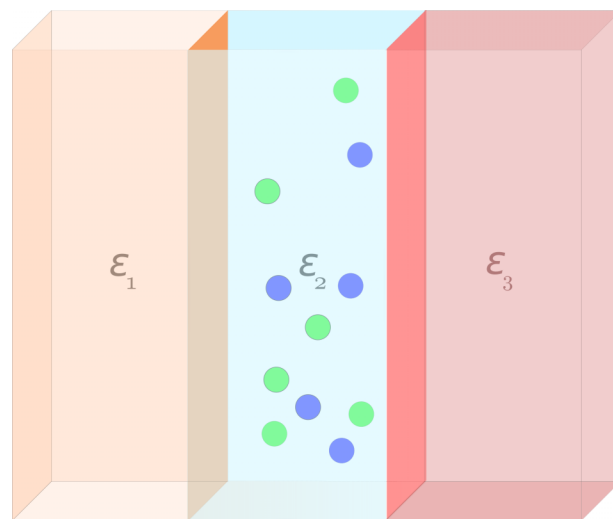


FIG. 1. Sketch showing three uniform dielectric regions of permittivities ϵ_1 , ϵ_2 , ϵ_3 separated by two sharp planar interfaces. The figure also shows the presence of finite-sized positive (blue) and negative (green) ions in the medium confined between the two interfaces. In the case of dielectric mismatch, the interfaces carry polarized charge. Coarse-grained models of this kind are often employed to study effective interactions between two bio-macromolecules or colloidal particles.

permittivities in the three regions (ϵ_1 , ϵ_2 , and ϵ_3 ; see Fig. 1). The effects of an external electric field on deforming the ionic structure are also studied. The case of zero dielectric contrast at both interfaces is simulated with standard MD simulations. For the simulation of ions in media with piecewise-uniform dielectric response, we employ a recently developed molecular dynamics method based on the Car-Parrinello idea⁴² of dynamical optimization that allows for a faster, accurate, and stable computation of dielectric effects via an on-the-fly evaluation of the induced charge at the dielectric interfaces.^{17,27} On the theoretical front, we evaluate the Ornstein-Zernike (OZ) equation with the (anisotropic) hypernetted chain closure (AHNC), based on the work by Kjellander and Marčelja,^{30,31} which has been applied recently to extract the fluid structure in confined geometries.^{18,32}

II. MODEL AND METHODS

A. Model

Our model system consists of an electrolyte solution confined within two planar surfaces (interfaces) parallel to each other (see Fig. 1).^{37,43} The surfaces are also uncharged, that is, we do not consider any free charges residing on the surface (except for the case where we introduce a uniform electric field that can be considered as arising from the presence of free charges on the two interfaces). The surfaces themselves are considered to be infinite in extent. Two scenarios are examined in detail. First, we model the interfaces as unpolarizable which allows us to isolate the roles of interionic steric interactions, ion-interface steric interactions, and ion-ion electrostatic interactions in determining the ionic density distribution in the solvent confined within the interfaces. Second, we model the scenario where the two interfaces can get polarized due to differences

in dielectric response of the media they separate. Further, we note that our system is closed, in other words, it is not in contact with an electrolyte reservoir. We highlight the role that induced charges at the interfaces play in deforming the ionic structure confined within the interfaces.

We choose $z = -H/2$ and $z = H/2$ planes as the interfaces and define H as the separation between them. For all the systems we study, $H = 3$ nm. We denote the $z = -H/2$ plane as interface I and $z = H/2$ plane as interface II. We often refer to interfaces I and II as left and right interfaces, respectively. We consider impermeable interfaces, that is, no transport of ions is allowed across the interface. In all cases, we consider the solvent confined within the planar interfaces (interior medium) to be water. In our simulations, the ions are modeled as (soft) spheres of radius σ that interact via a purely repulsive Lennard-Jones (LJ) potential. We choose $\sigma = l_B/2 = 0.357$ nm, where l_B is the Bjerrum length in water at room temperature. In our theoretical calculations, the ions are modeled as hard spheres of the same radius σ . For both methods of study, we model the interaction between an ion and the interface via the purely repulsive LJ potential. The ions also interact with each other and with the interface, in the case when the latter is polarizable, with a Coulomb potential. For unpolarizable interfaces, the Coulomb potential energy between two ions is given by $U_C = q_i q_j l_B / r_{ij}$, where q_i and q_j are, respectively, the charges on the ion i and ion j , and r_{ij} is the distance between those ions.

We consider both symmetric and asymmetric electrolytes and study the following stoichiometric ratios ($z_+ : z_-$)—1:1, 2:1, 3:1, and 0:0. Note that all our ions have identical sizes; we do not take into account possible differences in ionic sizes, for example, between a monovalent anion and a trivalent cation. The 0:0 study corresponds to a simulation with only LJ interactions and acts as a reference case aiding in the comparison between the effects of Coulomb interaction against the steric interactions. We perform simulations for average negative (monovalent) ion concentrations of 0.1, 0.5, and 0.9M. In all cases, the ions are present in the interior dielectric medium (water) with permittivity $\epsilon_2 = 80$. For the study of unpolarizable interfaces, the medium left to the interface I (left dielectric with permittivity ϵ_1) and the medium right to the interface II (right dielectric with permittivity ϵ_3) are taken to be water and we have $\epsilon_1 = \epsilon_2 = \epsilon_3 = 80$. For the study of polarizable interfaces, we study three cases ($\epsilon_1 | \epsilon_2 | \epsilon_3$): 20|80|20, 20|80|160, and 40|80|10. All simulations and theoretical calculations are performed at room temperature $T = 298$ K.

Unless otherwise stated, we express lengths in the units of σ —the ionic radius in our model ($=0.5l_B$). The unit of energy is $k_B T$, where k_B is the Boltzmann constant, and the unit of mass is chosen to be the ionic mass m . In these reduced units, time is measured in $\tau = (m\sigma^2/k_B T)^{1/2}$. The unit of charge is taken to be the charge of a proton e and we express concentrations and ionic densities in molar (M).

We employ this model to examine the deformation of the ionic structure near interfaces in response to changes in system attributes such as ion concentrations, ion valencies, external electric fields, and interfacial dielectric contrasts. In Subsections II B and II C, we provide the details associated

with the simulation and theoretical methods that are used to study the model system.

B. Molecular dynamics simulations

We simulate ions confined by the dielectric interfaces using MD methods. We account for the infinite extension of the interfaces in the simulation by considering periodic boundary conditions in the x and y directions. The whole system of ions and solvent confined within the two surfaces is taken to be in a rectangular simulation box of volume $V = H \times L \times L$, where L is a length that characterizes the size of the interface along the x and y directions. In all our simulations, L is taken to be significantly larger as compared to the ion radius σ and the Debye length λ_D in order to accurately simulate the unboundedness of the system in the x and y directions. The long range of the electrostatic potential is treated within the approximation of the minimum image convention and using the charged sheets method. The charged sheets method has been described in Refs. 44 and 45 and was employed in the simulation of the primitive model describing two immiscible electrolytes separated by a planar interface where it was found that the simulation results were in good agreement with experimental data.⁴⁶ As a check, we simulated the model systems by employing the 3D-Ewald sums with dipole corrections and the results were found to be nearly identical to those obtained using the charged sheets method. The length L is chosen to be large enough to minimize any errors that stem from the above approximate treatment of the long-ranged Coulomb interactions. The total number of dissociated electrolyte ions that enter our main simulation cell is $N = N_p + N_n$, where N_p and N_n are the total number of positive and negative ions, respectively. To impose the desired temperature in the system, we employ Nosé-Hoover thermostat chains.

In order to compare the three asymmetric electrolyte systems (1:1, 2:1, 3:1), we change the valency of positive ions keeping the average concentration of negative monovalent ions in the slit, $c_n = N_n/V$, fixed. Keeping c_n fixed across the three electrolyte systems generates distributions of positive ions with a relatively smaller spread in their volume fractions (as compared to the case if $c_p = N_p/V$ was held fixed). In addition, it generates all the three electrolyte systems with equal total positive charge (and equal total negative charge) which is distributed differently among the ions associated with 1:1, 2:1, 3:1 electrolytes. Thus, a fixed c_n enables us to attribute (for the most part) the differences in the ionic structure of the three systems to the differences in the valency of the positive ions and the associated changes in the electrostatic interactions. This allows us to accurately compare the contributions of electrostatic and hard-core interactions in determining the ionic distributions for the 1:1, 2:1, and 3:1 electrolytes. For the ease of presentation, we also use c_n to characterize the electrolytes, although it should be noted that for a $z_+ : 1$ electrolyte, the concentration is generally defined as N_p/V .

In Table I, we list the systems studied with MD simulations and the relevant parameters associated with their models. For the study of ions near unpolarizable interfaces, we

TABLE I. Model parameters and simulation variables.

$z_+:z_-$	c_n (M)	λ_D (σ)	L (σ)	N_p	N_n	N
1:1	0.1	2.69	96	212	212	424
	0.5	1.20	42.9	212	212	424
	0.9	0.89	32	212	212	424
2:1	0.1	2.20	96	106	212	318
	0.5	0.98	42.9	106	212	318
	0.9	0.73	32	106	212	318
3:1	0.1	1.90	96	71	213	284
	0.5	0.85	42.9	71	213	284
	0.9	0.63	32	71	213	284

use the standard MD simulation procedure. The ionic degrees of freedom are evolved using the velocity Verlet algorithm with a timestep $\Delta = 0.0005\tau$. Table I also provides the simulation details associated with this study for various concentrations c_n and stoichiometric ratios. Here, λ_D is the Debye length calculated assuming that the background dielectric is water; a large value of λ_D indicates a longer range for Coulomb interactions in the system. The length L is chosen much greater than λ_D in each case study.

In the case of polarizable interfaces, due to the presence of induced charges at the interface, the simulations incur a cost of meshing the interface with discrete finite elements to represent the induced charge density. This sets a limit on the simulation cell size L and for all the case studies with polarizable interfaces, we choose $L = 40\sigma$. As is evident from the values of the Debye length for various cases (see Table I), this choice for L is still much larger than λ_D . The number of positive and negative ions that enter the simulation cell is computed via the relations, $N_n \sim 367 \times c_n$ and $N_p \sim N_n/z_+$, where c_n is in molar.

The need to accurately compute the induced charges on the interfaces at every step of the simulation in order to correctly update the ionic configuration makes the use of conventional MD methods to extract equilibrium densities very time consuming and inefficient. Therefore, we employ a recently developed Car-Parrinello molecular dynamics (CPMD) method that allows the propagation of ionic degrees of freedom in tandem with an accurate update of the polarization charges at the interfaces.^{17,27} Our CPMD simulation scheme is based on the variational functional introduced in Ref. 17,

$$I[\omega] = \frac{1}{2} \iint \rho_r G_{\mathbf{r},\mathbf{r}'} (\rho_{\mathbf{r}'} + \Omega_{\mathbf{r}'}[\omega]) d\mathbf{r}' d\mathbf{r} - \frac{1}{2} \iint \Omega_{\mathbf{r}}[\omega] G_{\mathbf{r},\mathbf{r}'} (\omega_{\mathbf{r}'} - \Omega_{\mathbf{r}'}[\omega]) d\mathbf{r}' d\mathbf{r}, \quad (1)$$

where ρ and ω are the free and induced charge densities, respectively. The function $G(\mathbf{r},\mathbf{r}') = |\mathbf{r} - \mathbf{r}'|^{-1}$ is the bare Green's function and Ω is given by

$$\Omega_{\mathbf{r}}[\omega] = \nabla \cdot \left(\chi_{\mathbf{r}} \nabla \int G_{\mathbf{r},\mathbf{r}'} (\rho_{\mathbf{r}'} + \omega_{\mathbf{r}'} d\mathbf{r}') \right), \quad (2)$$

with χ being the dielectric susceptibility. The particular form for the functional in the case of two sharp, planar dielectric

interfaces is shown in the Appendix. In this form, $I[\omega]$ becomes a functional of the induced charge density residing at the interfaces.

The minimization of $I[\omega]$ leads to the equation, $\omega = \Omega$; the solution of this equation generates the correct induced density on the interfaces. Furthermore, owing to the fact that $I[\omega]$ is a true energy functional, it offers the possibility to be minimized dynamically, that is, we are allowed to perform a simultaneous update of the free charge (ionic) configuration and the induced charge densities on interfaces I and II. To do this, we include $I[\omega]$ as the potential energy part of the Lagrangian \mathcal{L} whose kinetic part includes the kinetic energy associated with the ions and a fictitious kinetic energy assigned to the surface induced charge density ω which is treated as a dynamical variable of mass μ . The value of μ is chosen so as to make the energy contribution of the fake degrees of freedom small. In practice, we choose these masses to be proportional to the areas of the finite elements employed to discretize the interface. Further details of the method can be found in Ref. 17.

We mesh each flat interface with $M = 484$ points generating a uniform grid of finite elements that are dressed with induced charges. The area per finite element is $L^2/M \sim 3.3\sigma^2$ which is roughly the same size as the effective cross-sectional area of the ion $\sim \pi\sigma^2$. Using the equations of motion derived from \mathcal{L} , we generate the dynamics for the whole system—ions and the fake degrees of freedom corresponding to the induced charge values, using the standard MD technique with a timestep $\Delta = 0.001\tau$. The ions couple to a Nosé-Hoover thermostat reservoir at temperature $T = 298$ K while the induced charge (fake) degrees of freedom couple to a second Nosé-Hoover thermostat at a much lower temperature $T_f = 0.002$ T. The value for fictitious mass μ depends on the particular system under study (concentration, stoichiometric ratios, etc.) and we find μ to fall in the range $\mu = 60$ –1000 to optimize the stability of the simulation. Finally, due to the overall electroneutrality associated with the system, the net induced charge at each interface vanishes. We enforce this constraint in each step of our CPMD simulation via the shake-rattle routine.⁴⁷

As mentioned above, in CPMD simulations, the amount of induced charge at a given interfacial grid point is treated as a dynamical variable and the overall system is described by an extended Lagrangian that includes the (fake) degrees of freedom associated with these induced charge variables in addition to the ionic degrees of freedom. As a result, a system with N ions confined by unpolarized interfaces effectively translates into a system with $2M$ additional degrees of freedom in the case of polarized interfaces (recall that M is the number of finite elements meshing each interface). As we do not employ any acceleration strategies such as Ewald sums or particle-mesh methods, the scaling associated with either of the MD methods employed is the typical $O(n^2)$ scaling characteristic of charge simulations. While the time complexity for the conventional MD simulation of ions confined by unpolarized interfaces is $O(N^2)$, the computational costs for CPMD simulations of ions confined by polarized surfaces scale roughly as $O((N + 2M)^2)$. Hence, on average, we find our CPMD simulations to be slower

than conventional MD simulations roughly by a factor of $(N/(N+2M))^2$. For instance, in the case of the CPMD simulations of monovalent electrolyte at $c_n = 0.5\text{M}$ with $N = 368$ ions and $M = 484$ grid points, the central processing unit (CPU) time is 61.4 ms per timestep while for the MD simulation of the same system (with unpolarized interfaces), the CPU time is 9.4 ms per time step. We note that these CPU times are for a simulation performed on a 16 core CPU node with OpenMP shared memory multiprocessing.

C. Liquid state theory

We base our theoretical method on the work of Kjellander and Marčelja's,^{30,31} referred to as the AHNC. The method is thoroughly and completely described in these articles, and subsequent works by these authors, and explains in detail how the OZ equation is solved in an inhomogeneous system of primitive model electrolytes in a planar confinement. A visual interpretation of the mathematical procedure is presented in the supplementary material of Ref. 18, together with a discussion of some characteristic results. The theory does not only focus on the 1-particle density profiles, as many density functional theories and field-theoretical approaches, but also allows for the calculation of the anisotropic pair-correlation functions. The only approximation in the method is the choice for the particular closure equation for the OZ equation, in this case the Hyper-Netted Chain (HNC). The pair-correlation functions $h(\mathbf{r}, \mathbf{r}')$ and $c(\mathbf{r}, \mathbf{r}')$ (respectively, the total correlation function h and direct correlation function c), are iteratively solved with the OZ equation

$$h(\mathbf{r}, \mathbf{r}') = c(\mathbf{r}, \mathbf{r}') + \int d\mathbf{r}'' c(\mathbf{r}, \mathbf{r}'') \rho(\mathbf{r}'') h(\mathbf{r}'', \mathbf{r}') \quad (3)$$

and the HNC closure

$$c(\mathbf{r}, \mathbf{r}') = h(\mathbf{r}, \mathbf{r}') - \ln(1 + h(\mathbf{r}, \mathbf{r}')) - u(\mathbf{r}, \mathbf{r}'), \quad (4)$$

for a given pair potential u (in our case, the Coulomb potential plus a hard core repulsion), and for a given particle distribution $\rho(\mathbf{r})$. We use dimensionless units for potentials, by dividing the potentials (in units of energy) by the thermal energy $k_B T$. The 1-particle distribution ρ is calculated with the (exact) Boltzmann distribution

$$\rho(\mathbf{r}) = \rho_0 \exp(-V(\mathbf{r}) - \mu_{\text{exc}}(\mathbf{r})), \quad (5)$$

with an external field V , and the excess chemical potential μ_{exc} (over the ideal contribution, i.e., due to pair-correlations), related to the logarithm of the activity coefficient. The excess chemical potential can be expressed in terms of the pair-correlation functions, for example, by solving the exact Lovett-Mou-Buff-Wertheim equation,³² or if one uses the HNC approximation to solve the OZ equation, one can use a specific expression that follows from that approximation,

$$\mu_{\text{exc}}(\mathbf{r}) = \rho(\mathbf{r}) \int d\mathbf{r}' \frac{1}{2} h(\mathbf{r}, \mathbf{r}') (h(\mathbf{r}, \mathbf{r}') - c(\mathbf{r}, \mathbf{r}')) - c(\mathbf{r}, \mathbf{r}'), \quad (6)$$

as derived in Ref. 48 and applied in the AHNC in Refs. 30 and 31.

The set of Equations (3)-(6) is solved iteratively, until self-consistency is achieved within a small numerical error. Equations (3) and (4) yield the pair-correlation functions h and c for a given ρ , and Equation (5) yields the density ρ for given pair-correlation functions h and c that are required to calculate the excess chemical potential, Equation (6). For notational convenience and readability, we have been omitting indices that denote particle type, but actually one would have to calculate the density ρ_i of each particle type i , and pair-correlation functions h_{ij} and c_{ij} between each pair of types i and j . In the AHNC, one discretizes the z -axis (the axis perpendicular to the planar boundaries) and labels the densities according to the distance z_k with an additional index k , and likewise, the pair correlation functions with two indices. A more complete notation of a correlation function could look like $h_{ij}(z_k, z_l, r)$, denoting the total pair correlation between a particle of type i at position z_k and one of type j at z_l , with cylindrical coordinate r (parallel to the boundaries) separating the pair. The procedure is exactly as described above, except that the equations become (high-dimensional) matrix equations. Again, Refs. 30 and 31 provide a complete description, with some application and interpretation in, e.g., Refs. 18 and 49.

The Coulombic part of the pair-potential should satisfy Poisson's equation. In the presence of different dielectric boundaries, we use the so-called method of images to achieve this. The result of this method is an infinite summation of Coulomb potentials $\propto \sum 1/r_i$ (that decay with the inverse of the distance r_i) between the particles within the slit, and between the particles and their infinite set of images.¹⁸ The interaction between a particle and all its images can be interpreted as an external force acting on the particle, $V_{\text{pol}}(z)$, that depends on the dielectric contrast, distance to the boundary, and separation between the boundaries.¹⁸ The infinite sum of the image contributions is evaluated in k -space and yields an exact expression,^{18,30}

$$V_{\text{pol}}(z) = \frac{q^2 l_B}{H} \ln(1 - A_{12} A_{13})^{-1} + \int_0^\infty dk q^2 l_B \left(\frac{A_{12} e^{(H-2z)k} + A_{13} e^{(2z-H)k}}{1 - A_{12} A_{13} e^{-2Hk}} \right) \quad (7)$$

with $A_{ij} = (\epsilon_i - \epsilon_j)/(\epsilon_i + \epsilon_j)$ being the dielectric contrast between medium i and j , and H being the separation between the interfaces. The interaction between a particle and the images of another particle is included in the total pair-potential u . For the interaction between the ion and the interfaces, we use a "soft" Lennard-Jones repulsive potential, the same potential as in the case of the simulations,

$$U(z) = 1 + \sum_{l=1,2} 4 \left(\left(\frac{\sigma}{|z - z_l|} \right)^{12} - \left(\frac{\sigma}{|z - z_l|} \right)^6 \right), \quad (8)$$

for $|z - z_l| < 2^{\frac{1}{6}} \sigma$ with z_l being the location of the interfaces. Otherwise, the particles are treated as perfectly hard spheres with a positive or negative charge. We expect this difference in the treatment of the short range repulsion to contribute towards small differences between the results of the CPMD and the AHNC. The electrostatic attractions could enable the

ions to overcome a small region of the steep LJ-repulsion. The distance of closest approach is therefore smaller between oppositely charged ions with a LJ repulsion than between two ions with a perfectly hard core. This would result in a slightly stronger electrostatic coupling between LJ particles than between two hard spheres with a same diameter.

III. RESULTS

A. Unpolarizable interfaces

We begin by presenting our simulation and theoretical results for the case of ions confined within unpolarizable planar interfaces that separate media of the same dielectric (water) on either sides. We first show how the equilibrium ionic structure in these systems deforms upon changing the stoichiometric ratio (ion valency) and/or electrolyte concentration. The ionic structure is represented by the number density n_z of ions in the z direction (in molars) and in some cases by their charge density ρ_z (in units of eM). In all our plots, we show this density as a function of the z coordinate in nanometers.

1. Effect of ion valency and concentration

In Fig. 2, we plot the density profiles of positive ions for a $z_+:1$ electrolyte ($z_+ = 1, 2$, and 3) with concentration $c_n = 0.1M$. Note the reduction in the total number of positive ions as the valency of the positive ions is increased due to the constraint of electroneutrality. We find that the MD results and the AHNC lines are in good agreement aside from a small discrepancy at distances very close to either interfaces. We attribute this mismatch to the differences in the modeling of ions in the two approaches. While in MD simulations, we model ion-ion steric interactions via soft LJ forces, for the AHNC calculations, these interactions are treated as hard-sphere interactions.

For the 1:1 electrolyte, we find the ion density (red squares) peaks near the interfaces as Fig. 2 shows. This implies that the positive ions corresponding to the 1:1 electrolyte tend to accumulate near the interfaces. This accumulation, as will be demonstrated later in this section, is the result of stronger

steric interactions between the ions which dominate the weak interionic Coulomb interactions between the monovalent ions. Further, we observe the presence of a weak modulation in the density profile near the center of the confinement. As we will soon see, this modulation or layering in the ionic structure becomes more prominent as the average ion concentration is increased. The situation is different for the 2:1 and 3:1 electrolytes. We find that the multivalent ions associated with these electrolytes are depleted near the interface with the depletion more pronounced in case of the trivalent cations (blue triangles) as compared with the divalent ones (green circles). We attribute this depletion to stronger ionic correlations that are present in the case of multivalent ions. A graphic description of the microscopic mechanisms is shown in Sec. IV.

We next show the results for the same systems as above but with higher electrolyte average concentrations. In Fig. 3, we plot the ion density profiles for the case where $c_n = 0.5M$. Once again we observe a good agreement between MD (symbols) and AHNC (dashed lines) results with minor differences in the density values closer to the interface. We find that for the 1:1 electrolyte, the accumulation of ions (red squares) is enhanced near the interfaces as compared to the case of $c_n = 0.1M$. We attribute this enhancement to the stronger steric effects present in the ionic system at $c_n = 0.5M$. While in the $c_n = 0.1M$ case, we observed a depletion in the ionic density of the 2:1 electrolyte close to the interface, for $c_n = 0.5M$ electrolyte, the ion density of divalent ions (green circles) is enhanced near the interface which indicates the dominance of steric interactions over the Coulomb interactions. This competition between steric and electrostatic forces is seen to also produce the nearly flat (constant) density profile of trivalent ions (blue triangles) near the interface in the case of 3:1 salt in stark contrast to the situation in Fig. 2. In the $c_n = 0.1M$ case, the Coulomb interactions were sufficient to wash out the layered structure for 2:1 and 3:1 electrolytes. On the other hand, at $c_n = 0.5M$, we observe that the modulations in the ionic structure for these electrolytes are more pronounced.

Fig. 4 shows the ionic density profiles for the same system at concentration $c_n = 0.9M$. We only show the densities

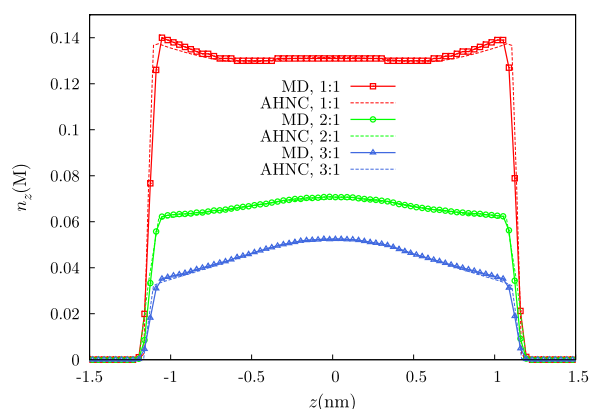


FIG. 2. Density n_z of positive ions for an electrolyte at $c_n = 0.1M$ confined within two unpolarizable planar interfaces. Symbols correspond to MD results and dashed lines to AHNC calculations.

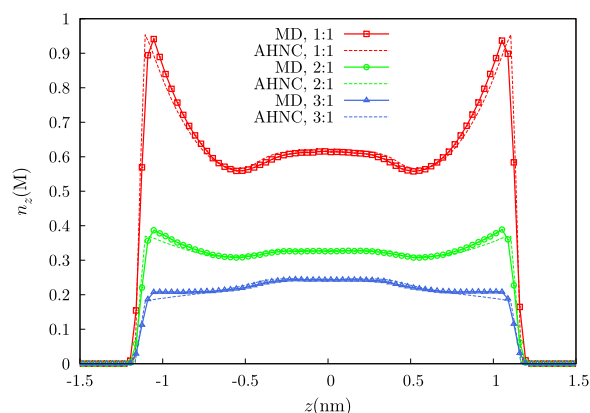


FIG. 3. Density n_z of positive ions for an electrolyte at $c_n = 0.5M$ confined within two unpolarizable planar interfaces. Symbols correspond to MD results and dashed lines to AHNC calculations.

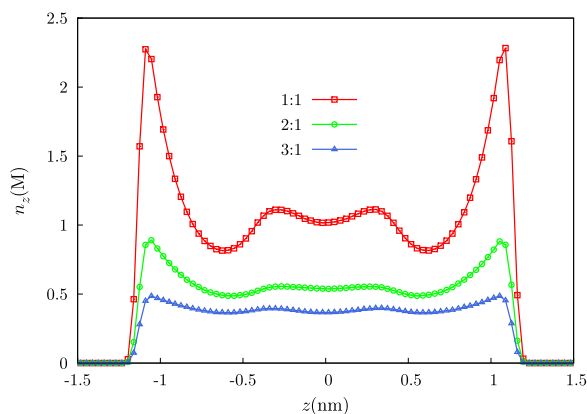


FIG. 4. Density n_z of positive ions for a electrolyte at $c_n = 0.9\text{M}$ confined within two unpolarizable planar interfaces obtained from MD simulations.

generated via MD simulations as at this concentration, we find it more difficult to converge the AHNC, and other closures may be more effective.^{32,50,51} We find that the trend of higher accumulation near interfaces upon increasing c_n continues. For 1:1 electrolyte (red squares), the ions strongly prefer to assemble near the interfaces. The accumulation near the interfaces for the 2:1 electrolyte (green circles) is further enhanced as compared to the $c_n = 0.5\text{M}$ case. More importantly, we find that the strong steric effects at $c_n = 0.9\text{M}$ dominate the Coulomb interactions even for the 3:1 electrolyte. As Fig. 4 shows, we find enhanced accumulation of trivalent cations (blue triangles) close to the interfaces in stark contrast to the $c_n = 0.1\text{M}$ case where electrostatics causes ion depletion near the interfaces. Furthermore, we find that at this concentration, for all three stoichiometric ratios, the modulations in the ionic structure become very prominent as compared to the aforementioned results at lower c_n .

It is useful to isolate and analyze the roles of steric and Coulomb interactions to understand why in the above studied systems the ions distribute as shown in Figs. 2–4. To achieve this, we turn off the charge on the ions in our simulations and obtain the densities for “ions” interacting via only the purely repulsive LJ forces. In other words, we replace both the positive and negative ions with electroneutral particles. We denote this system as the 0:0 electrolyte for the sake of brevity. In Fig. 5, we show the density profiles for this system at different concentrations $c_n = c_p = 0.1, 0.5$, and 0.9M . The plots confirm our earlier assertion that the accumulation of ions near the interfaces is the result of strong steric interactions. Furthermore, we find that the densities of 0:0 electrolyte at $c_n = 0.9\text{M}$ (blue triangles), $c_n = 0.5\text{M}$ (green circles), and $c_n = 0.1\text{M}$ (red squares, see inset) are nearly identical to the densities of 1:1 electrolyte at the same concentrations (red squares in Figs. 2–4), implying that the distribution of ions for the 1:1 case is largely determined by steric interactions. In addition, we find that the layering (modulations) of the ionic structure observed at the higher concentrations in Figs. 3 and 4 is indeed driven by steric interactions as similar modulations are seen in Fig. 5 at those concentrations as well.

By comparing the densities for the 2:1 and 3:1 multivalent salts with the plots in Fig. 5, we find that electrostatic forces dramatically alter the situation in these cases with

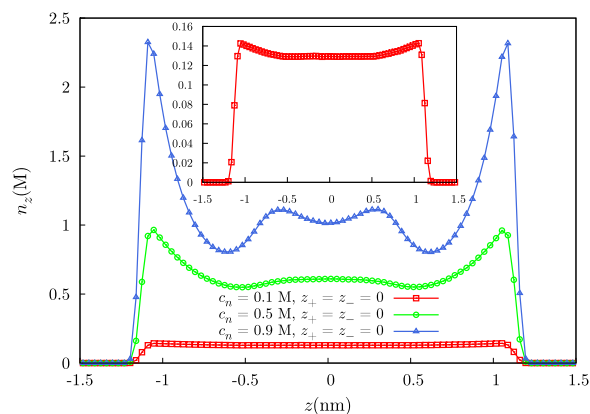


FIG. 5. Density of particles obtained from MD simulations for a 0:0 electrolyte (no electrostatic forces) at concentration $c_n = c_p = 0.1, 0.5$, and 0.9M confined within two unpolarizable planar interfaces.

their primary effect being to cause depletion of ions from the interfacial region as asserted before. For $c_n = 0.1\text{M}$, electrostatics clearly dominates over the steric interactions leading to a fully depleted ionic density profile for the multivalent ions near the interfaces (see Fig. 2). For higher concentrations of $c_n = 0.5$ and 0.9M , the two forces are more evenly matched and in some cases (see, for example, the density of trivalent ions at $c_n = 0.5\text{M}$ in Fig. 3), they appear to more or less cancel each other leading to a nearly uniform looking profile. In summary, we find that the steric interactions push the ions towards the interfaces and drive the layering (modulations) of the ionic structure while Coulomb forces deplete the ions from the interfacial regions. The competition between these two forces, tuned to varying degrees by controlling parameters such as the concentration or ion valency, leads to a rich gallery of equilibrium ionic structures confined within the planar interfaces.

2. Effect of electric field

In electrochemical capacitors, the charging process creates a potential difference between the parallel plates which drives the ions present in the electrolyte towards the plate surfaces leading to the formation of electrical double layers (EDLs).^{52–54} The capacitive power of such devices comes from the energy stored in the EDL. Thus, in order to understand the physics of EDL formation and suggest improvements in the design and working of such devices, it is important to study the effects of an external electric field on the ionic structure formed in the electrolyte under confinement. Such a study also aids in understanding the effective forces between charged colloids in the presence of electrolyte ions.⁵

We introduce a uniform electric field pointing from the right to the left interface. Its strength is measured by the potential difference V between the two interfaces. We analyze the ionic distributions of a 2:1 electrolyte with a concentration of $c_n = 0.5\text{M}$ at $V = 10, 50$, and 100 mV . In Fig. 6, we plot the charge densities (not the number densities) for positive ions, negative ions, and all the ions. The results for $V = 0$ case (depicted in Fig. 3) are also plotted for the sake of comparison. We first note that for all cases, the center of the slit (near $z = 0$)

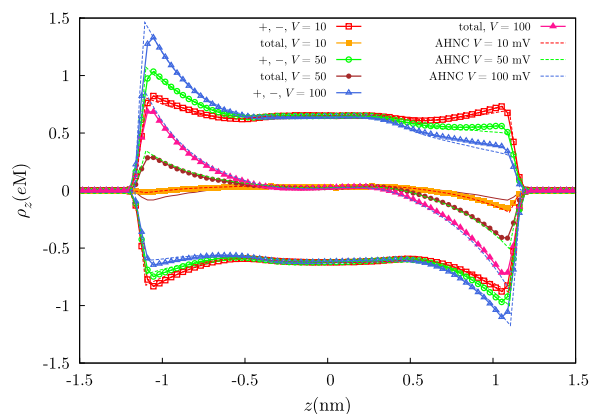


FIG. 6. Charge density ρ_z of positive ions, negative ions, and all ions as a function of z for a 2:1 electrolyte at $c_n = 0.5M$ confined within two unpolarizable planar interfaces. The effect of increasing the external electric field (applied by creating a potential difference V between the two interfaces) is shown for $V = 10, 50, 100$ mV. The brown solid line is the total charge density at $V = 0$ mV (no external electric field). Symbols are MD simulation results and dashed lines are AHNC results.

is electroneutral, that is, it is populated with ions such that the net charge vanishes in the region. Next, we find that for $V = 10$ mV, the densities are very similar to the case of neutral boundaries (no electric field) and we only observe a slight accumulation of positive ions on the left interface. However, in the total charge density, we observe a slight asymmetry in the distribution about the $z = 0$ plane, finding a net negative charge near the right interface which is not balanced by a net positive charge on the left interface, but by a very wide peak of positive charge in the center of the slit. We attribute this to the inherent bias of the neutral system (for 2:1 salt at $c_n = 0.5M$) towards a net negative total charge density near the interface as shown by the brown solid line near $\rho_z = 0$. We note that a mean field theory like Poisson-Boltzmann theory would predict a perfect anti-symmetric density profile for such a system.

As the potential difference between the two plates is increased to 50 mV, we see a more clear separation of ions in the system. The accumulation of positive ions in the neutral case near the right interface is now suppressed almost completely by the electric field working against it. The (absolute value of) charge density for the negative ($z_- = -1$) ions is still found to be maximum near the interfaces. The total charge density reflects the separation of charge with a near-antisymmetric distribution of ions. For $V = 100$ mV, the effects of electric field are the strongest of the studied cases which is to be expected. The positive ions prefer the left interface while the negative ions are accumulated on the right. A clear separation of net charge is seen in the total density which has an antisymmetric form about the $z = 0$ center plane.

In Fig. 7, we plot the charge density of positive ions associated with 1:1, 2:1, and 3:1 electrolyte which is in the presence of an electric field corresponding to a potential difference of 100 mV between the left and right interfaces. The concentration is $c_n = 0.5M$ for all systems. We first find that the charge density near the $z = 0$ region increases as the valency of the positive ions is incremented. Note that for a fixed stoichiometric ratio, as Fig. 6 shows, the charge

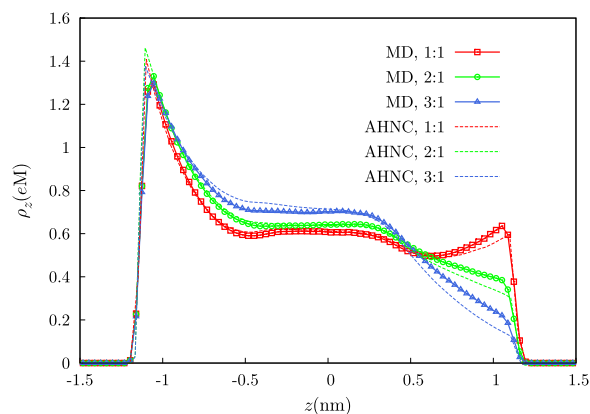


FIG. 7. Charge density of positive ions for a $z_+:1$ electrolyte at $c_n = 0.5M$ and under the influence of an external uniform electric field corresponding to a 100 mV potential difference between the two interfaces and pointing from the right to the left interface. Interfaces are considered unpolarizable. Symbols are MD simulation results and dashed lines are AHNC calculations.

density near the central region remained unaffected by an increase of the electric field strength. Next, we observe that the electric field is strong enough to push the positive ions towards the left interface. The peak value of the density near the left interface is seen to be independent of the valency of positive ions. Near the right interface, the charge density shows a much stronger dependence on z_+ . We find that for the 1:1 electrolyte, the positive ions still accumulate near the right interface against the potential gradient. Recall that for the same system with neutral boundaries (that is without the electric field, see Fig. 3), ions preferred to assemble near the interfaces, a finding that was attributed to the stronger steric forces at $c_n = 0.5M$. It appears that this accumulation is not suppressed for the 1:1 case even with the potential bias of 100 mV. On the other hand, for the 2:1 and 3:1 electrolytes, the density plots show ion depletion near the right interface in contrast with the profiles that showed peak accumulation near the interfaces in the case of neutral boundaries. The depletion for trivalent cations is found to be stronger as compared with the divalent ions.

B. Polarizable interfaces

We now study systems with polarizable planar interfaces, in other words, with interfaces that separate media of different dielectric permittivities on either sides.^{37,43} We consider three different cases ($\epsilon_1|\epsilon_2|\epsilon_3$): case (i) = 20|80|20, case (ii) = 40|80|10, and case (iii) = 20|80|160, where ϵ_1 , ϵ_2 , and ϵ_3 are the dielectric constants of left, central, and right media, respectively (see Fig. 1). These three examples are chosen to showcase the different effects that can arise due to the two polarizable interfaces. In the 20|80|20 case, we expect the interfaces to cause depletion of the density near the interface with a symmetric final density profile owing to the equal dielectric contrasts at the two interfaces. The case of 40|80|10 introduces the element of asymmetric depletion from the left and the right interfaces. The third scenario with 20|80|160 is considered to introduce the possibility of one interface repelling the ions and the other attracting them.

For each of these cases, we investigate how the equilibrium ionic structure deforms upon changing the stoichiometric ratio and/or electrolyte concentration. The simulation results are obtained from CPMD method outlined in Sec. II B where the averages for the ion densities are computed from runs with nearly 30×10^6 steps (timestep $\Delta = 0.001\tau$). While the polarization charge is treated in a discrete manner in the CPMD method, it is considered continuous in the AHNC method. The infinite sum of image charge contributions can be performed conveniently in k -space and results in a single exact expression. The AHNC therefore provides a reference for potential effects caused by the discretization of the polarization charge in the CPMD. Once again, we represent the ionic structure by the number density of ions in the z direction and show this density in molar as a function of the z coordinate in nanometers.

1. Low salt concentration: $c_n = 0.1\text{M}$

In Fig. 8, we plot the density profiles of positive ions for a $z_+:1$ electrolyte ($z_+ = 1, 2$, and 3) with a concentration of $c_n = 0.1\text{M}$ and dielectric configurations of 20|80|20, 40|80|10, and 20|80|160, respectively. We find that the CPMD predictions and AHNC results are in very good agreement. Recall that for this same system with unpolarizable interfaces, we found the monovalent positive ions assembling near the interfaces while the divalent and trivalent ions stayed away from the interfaces (see Fig. 2). From Fig. 8(a), we see that the density of monovalent ions (red squares) is depleted near the interfaces for the 20|80|20 system. Further, we find that the depletion of multivalent ions (green circles for divalent ions and blue triangles for trivalent ions) is stronger as compared with the unpolarizable interface case. This enhanced depletion is due to the fact that the ion in water (central medium) induces a charge on either interfaces of the same sign because of the lower dielectric constants of media adjacent to the central medium. This same charge repulsion reinforces the already present depletion due to strong electrostatic ion-ion correlations which is sufficient to overcome the accumulation near the interfaces favored by the steric forces for the case of monovalent ions. Additionally, we find that the profiles for the 20|80|20 are symmetric about the $z = 0$ plane as in Fig. 2.

We next examine the density profiles for the 40|80|10 system which are shown in the plot of Fig. 8(b). We first notice the asymmetric nature of the densities owing to the different values for the dielectric contrasts at the left (40|80) and the

right (80|10) interfaces. As the dielectric media adjacent to the central region still have a lower dielectric constant, we find the ionic density profiles to be depleted relative to the unpolarizable interface case. We find that due to a stronger contrast at the 80|10 (right) interface, the depletion is stronger near it as compared with the 40|80 (left) interface. The density for monovalent ions (red squares) near the left interface is nearly uniform implying that the depletion of ions near the interface caused by the repulsion due to the induced charges at this interface is not so strong to completely overcome the accumulation caused by the steric interactions. Next, in Fig. 8(c), we show the profiles for 20|80|160 case. Here, while the left polarized interface causes ions to repel away from the interface, the right interface attracts them owing to fact that the medium right to the central medium has a higher dielectric constant and thus leads to the induction of a charge of opposite sign on the interface due to the ion in water. Hence, we find that the density profiles show an accumulation near the right interface and depletion near the left one, the depletion becoming stronger with rising z_+ . Unlike Figs. 8(a) and 8(b), we observe an additional non-monotonicity in the density profile for the multivalent ions where the density starts to first drop as one moves away from the central ($z = 0$) region and then rises again close to the right interface.

2. High salt concentration: $c_n = 0.5\text{M}$ and $c_n = 0.9\text{M}$

We next show the results for the same systems as above but at higher electrolyte concentrations. Here, the effects due to the polarized interfaces are similar to the above discussed case of $c_n = 0.1\text{M}$, and hence, we will be brief in their description, although, in contrast to the previous case, the effects may be secondary to the effects of the ionic correlations.

In Fig. 9, we plot the ion density profiles for the case where $c_n = 0.5\text{M}$. Once again the agreement between CPMD (symbols) and AHNC (dashed lines) results is good with minor differences in the profiles closer to the interfaces. Recall that for this system with unpolarizable boundaries, we observed that monovalent and divalent cations preferred to be near the interfaces while the trivalent ions stayed away from the interfaces, and we also saw enhanced modulations in the ionic structure (see Fig. 3). We find a similar overall trend for the density of monovalent ions (red squares) for all the three systems with polarizable interfaces studied, with some subtle differences near the interfaces which arise due to the induced charge repulsion or attraction as explained above. On

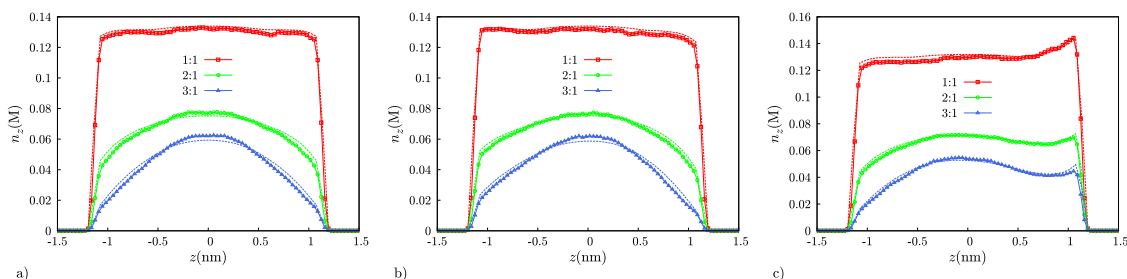


FIG. 8. Density n_z of positive ions for a $c_n = 0.1\text{M}$ electrolyte confined within two polarizable planar interfaces with dielectric profile (a) 20|80|20, (b) 40|80|10, and (c) 20|80|160 (see text for the meaning of the notation). Symbols correspond to CPMD results and dashed lines to AHNC calculations.

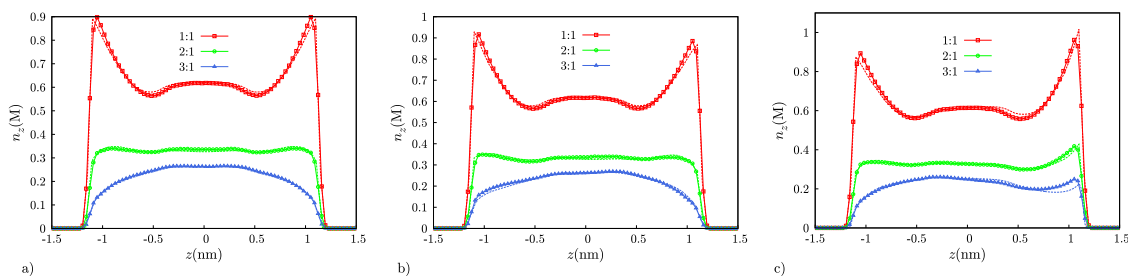


FIG. 9. Density n_z of positive ions for a $c_n = 0.5\text{M}$ electrolyte confined within two polarizable planar interfaces with dielectric profile (a) 20|80|20, (b) 40|80|10, and (c) 20|80|160 (see text for the meaning of the notation). Symbols correspond to CPMD results and dashed lines to AHNC calculations.

the other hand, for the divalent ions (green circles), we find that the dielectric effects are strong enough to alter the density profiles obtained for unpolarizable boundaries. In the case of 20|80|20, the density is depleted very close to the interface (see Fig. 9(a)) and appears to exhibit more modulations relative to the unpolarized systems. For the 40|80|10 system, as Fig. 9(b) shows, the density is depleted near the right interface (strong induced charge effect) and rises near the left interface (weak induced charge effect unable to overcome steric effects) in accordance with the induced charge effects suggested by the dielectric contrasts at the two interfaces. Finally, for the 20|80|160 case, we find that the divalent ion density peaks near the right interface and is suppressed close to the left interface in alignment with our expectations from the dielectric response of the two interfaces (see Fig. 9(c)). In the case of 3:1 salt (blue triangles), we find that the ion-ion electrostatic forces and the Coulomb (dielectric) interactions between the ions and the interfaces dominate the ionic structure near the interfaces in all the dielectric profiles studied.

Figure 10 shows the ionic density profiles for the same system as analyzed above but now with a concentration $c_n = 0.9\text{M}$. We only show the densities generated via CPMD simulations. We find that for the monovalent and divalent ions, the effects of polarizable interfaces on the density profiles are weak and the steric interactions dominate the physics at this concentration as they did in the case of the unpolarized interfaces at $c_n = 0.9\text{M}$ illustrated by Fig. 4. Ion accumulation near interfaces for 1:1 and 2:1 salts is seen across the board with the polarized interface only slightly diminishing or enhancing the density near the interface based on the sign of the induced charge. Further, the modulations in the ionic structure for these systems continue to be present in the case of polarized interfaces as well. We find that the dielectric contrasts mainly influence the structure of trivalent cations (blue triangles) close to the interfaces. In stark contrast

to the $c_n = 0.9\text{M}$ case with no dielectric contrasts where steric interactions cause ion accumulation near the interfaces for 3:1 electrolyte (see Fig. 4), we find that the repulsion due to induced charges in conjunction with the existing ion-ion electrostatic forces causes the suppression of the density close to the interfaces for 20|80|20 and 40|80|10 systems and near the 20|80 interface of the 20|80|160 system. In addition, the overall density of trivalent cations appears to be nearly uniform in between the interfaces aside from the strong rise seen near the 80|160 interface for the 20|80|160 system.

IV. DISCUSSION

A. Structural features from ion-ion correlations

Figures 2-5 show several structural features in the ion density profiles that become more pronounced with ion concentration and valency. Ions are found to deplete from the boundaries, adsorb to the boundaries at higher concentrations, and show density oscillations at high concentrations. The forces that govern these structural features are not directly exerted by the boundaries, which are charge neutral and dielectrically matched in Figures 2-5, but arise from the thermal motion of the ions and the geometric constraints that the boundaries impose.

The explanation for the adsorption behavior can be understood by investigating the average local environment of an ion. In addition to yielding density profiles that are in close agreement with the MD and CPMD simulations, the AHNC also calculates the anisotropic pair correlation functions between the ions. These functions yield direct information about the mean forces that the ions experience between the boundaries, resulting from a combination of thermal motion and direct interactions. The main assumption of mean field theories is to put these forces to zero by assuming the pair

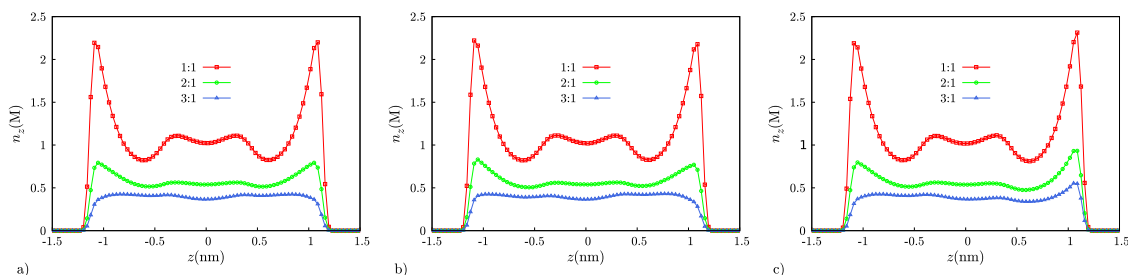


FIG. 10. Density n_z of positive ions for a $c_n = 0.9\text{M}$ electrolyte confined within two polarizable planar interfaces with dielectric profile (a) 20|80|20, (b) 40|80|10, and (c) 20|80|160 (see text for the meaning of the notation). Symbols correspond to CPMD results.

correlation functions to be constant. Such theories will therefore never distinguish the structural features of Figures 2-5, and many widely applied Poisson-Boltzmann theories, for example, would predict uniform ion density profiles. Still it is possible to refer to the seminal work of Debye and Hückel to explain the features in a qualitative fashion. However, for quantitative predictions and a more complete picture of the phenomenology, it is necessary to invoke the AHNC.

For a qualitative explanation, it is sufficient to know that electrolytes in a charged fluid are on average surrounded by compensating opposite charge. The “cloud” of screening charges (the “double layer”) is spherical in bulk by symmetry arguments but needs to deform close to a hard boundary because the cloud cannot penetrate the boundary. In what follows, we consider the 3:1 electrolyte at $c_n = 0.5\text{M}$ as an example system to discuss our explanation. Similar arguments can be invoked for all the other systems studied. Figure 11 shows the average charge distribution around an ion near the boundary (effect I). The asymmetric screening cloud exerts a force on the central ion, away from the boundary, resulting in an average depletion from the boundary. This (microscopic) depletion mechanism, which we attribute to electrostatic interactions, would apply to confined ionic fluids in general, except that its effect may be additive to those of other mechanisms. A second mechanism, driven

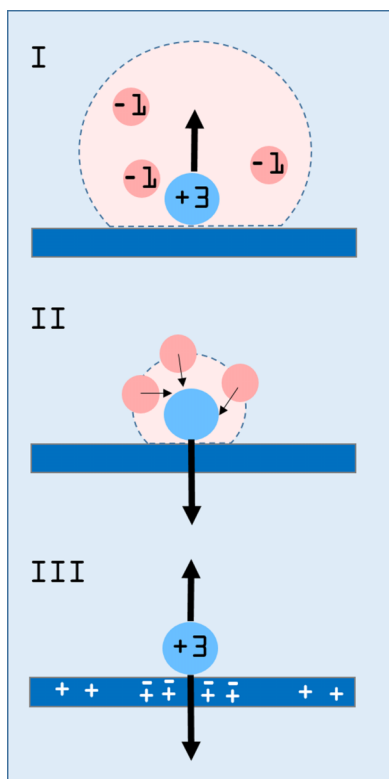


FIG. 11. Mean forces acting on an ion near a dielectric boundary. Deformation of the double layer tends to pull ions away from the boundary (effect I), but steric interactions tend to push ions against the boundary (effect II). Surface charge and polarization charge can attract or repel ions, depending on the relative sign of the charges (effect III). We find that effects I and II, which are absent in mean field theories, can compete with and overcome surface charge effects (effect III). The effects are shown for a 3:1 electrolyte, but apply to both symmetric and asymmetric electrolytes.

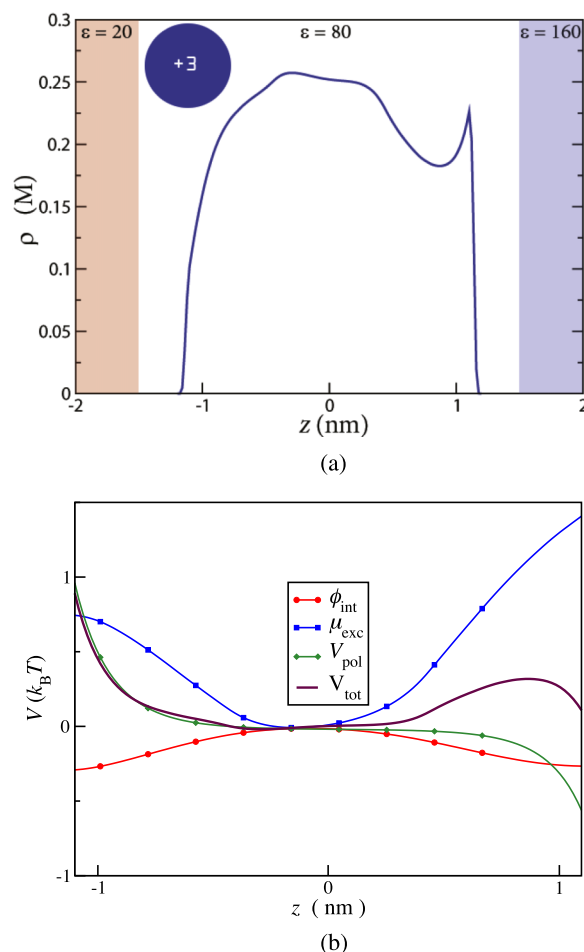


FIG. 12. Concentration profile of trivalent ions in a 3:1 electrolyte with a mean concentration of $c_n = 0.5\text{M}$, in a slit with dielectric profile 20|80|160 (a). The corresponding potentials acting on the trivalent ions are shown separately, calculated by the AHNC (b). The electric potential generated by local charge segregation is shown as the red line ϕ_{int} . Charge segregation is driven by the excess chemical potential μ_{exc} resulting from electrostatic and steric correlations (effects I and II in Figure 11), and V_{pol} , the polarization charge at the boundaries (effect III in Figure 11). The total potential is the sum of the contributions, $V_{\text{tot}} = 3\phi_{\text{int}} + \mu_{\text{exc}} + V_{\text{pol}}$. The mean potential from ionic correlations can overcome that of the polarization charge, $|\mu_{\text{exc}}| > |V_{\text{pol}}|$, typically at higher concentrations.

by steric interactions, is related to the volume fraction of ions or, in other words, to their entropy. Adsorption of ions increases the free volume of the remaining ions, which can be entropically favorable at high densities. An alternative way to rationalize the adsorption is to realize that ions near the boundary experience more collisions with other ions towards the boundary than away from it, resulting in a mean force towards the boundary (effect II of Fig. 11). Both effects are visible in Fig. 12. The potential ϕ_{int} is the electrostatic potential that is caused by the mean segregation of charge, obeying Poisson's equation corresponding to a planar geometry,

$$\phi_{\text{int}}(z) = -2\pi l_B \int dz' Q(z')|z - z'| \quad (9)$$

with $Q(z')$ being the total charge density at z' in particles per volume. The potential V_{pol} is the electrostatic potential generated by the polarization charge and is obtained by the method of images, given by Equation (7). The excess

chemical potential μ_{exc} is the mean potential that an ion experiences from the average interactions with the other ions, subtracted by the mean potential ϕ_{int} . The expression is given in Equation (6). By defining μ_{exc} in this way, it measures a mean potential purely caused by the local ordering of charge. The total potential that a trivalent ion experiences is the sum of these contributions: $V_{\text{tot}}(z) = V_{\text{pol}}(z) + 3\phi_{\text{int}}(z) + \mu_{\text{exc}}(z)$. For the parameters of a 3:1 electrolyte, the variation in the excess chemical potential μ_{exc} is larger than the variation in the mean potential ϕ_{int} . This demonstrates the importance of calculating the anisotropic correlation functions that are required to get an accurate value for μ_{exc} , as opposed to a majority of mean field methods that ignore the existence of μ_{exc} and solve for ϕ_{int} in a self-consistent manner. For the trivalent ions, the effect of μ_{exc} is also opposite to that of ϕ_{int} and contributes to the spontaneous formation of a double layer near the boundaries. Although the double layer near the boundary is unfavorable from a global perspective of ion entropy and electrostatic energy (ϕ_{int}), it is compensated by a more favorable local configuration of charge (μ_{exc}), because the trivalent ions are more favorably screened in the center of the slit. The electrostatics-driven depletion is found to increase with density and valency, with a range corresponding to the electrostatic correlation length (which decreases with density). The hard-core-driven adsorption is found to increase sharply at high densities, with a range corresponding to the ion size.

We ascribe the oscillations in the ionic density to a balance between two mechanisms: a maximization of free volume (entropy) and minimization of total electrostatic energy. In a recent work, Nygård *et al.* investigated density oscillations of a hard sphere fluid in a narrow slit.³² In our case, the Coulomb interactions enrich the phenomenology, but at high densities, we see similar effects, especially for monovalent ions.

Figures 8-10 show the additional influence of surface polarization. This effect has been analyzed in many contexts and is often approached with the “method of images.” Figures 8-10 show however that it is a secondary effect at higher ion concentrations⁵⁵ which only slightly modifies the structure imposed by ionic correlations (effects I and II in Figure 11). At the same time, the spatial variation of the dielectric properties of the environment, particularly in the case of electrolytes with low concentrations and multivalent ions, was found to have profound effects on the ionic structure. Hence, coarse-grained models and associated theoretical/computational procedures to study charged soft matter systems should include dielectric heterogeneities to accurately capture the physical properties of these materials.

B. Features in the total charge density

We point out another important feature of the ionic structure that, for the sake of brevity, we did not discuss in Sec. III. It is tempting to conclude, especially in the case of neutral, unpolarizable boundaries, that while the rich variations in the density profile for the positive ions of a $z_+:1$ electrolyte can be expected as a result of the aforesaid competition between electrostatic and steric interactions, the total charge density should be featureless owing to

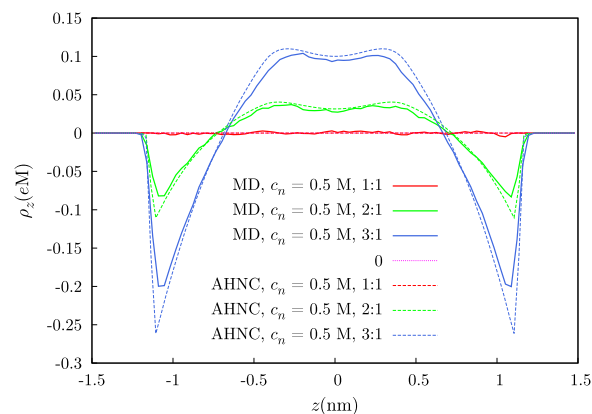


FIG. 13. Charge density corresponding to all the ions in the system for a $z_+:1$ electrolyte at concentration $c_n = 0.5\text{M}$ within two unpolarizable planar interfaces with dielectric profile 80|80|80 (see text for the meaning of the notation). Solid lines are MD results and dashed lines correspond to AHNC calculations.

the cancellations coming from the considerations of both positive and negative ions. Indeed, Poisson-Boltzmann theory and many of its modifications⁵⁶ would predict a uniform distribution coincident with the $\rho_z = 0$ line for the charge density of the total number of ions. This was found to be the case in our AHNC and MD calculations for the 1:1 electrolyte system at all concentrations where the result is to be expected from symmetry considerations as well. As Fig. 13 shows, our AHNC calculations found that the total charge density ρ^t was identically zero everywhere and our MD result for ρ^t was seen to fluctuate around zero, the small deviations from zero arising from the statistical noise present in the simulations. However, deviations from mean field theory predictions were observed for total charge densities of systems with asymmetric electrolytes containing multivalent ions.^{57,58} We found features in ρ^t similar to those seen in the density of positive ions n_z in the figures shown in Sec. III A 1 with the modulations in the density and the depletion/accumulation near the interfaces becoming significant as c_n increased. For example, in Fig. 13, we show the total charge density as a function of z for 1:1, 2:1, and 3:1 electrolytes at $c_n = 0.5\text{M}$. Clearly, for the 2:1 and 3:1 systems, the ionic structure is not washed out because of the cancellations predicted by a mean field approach. Since the steric interactions in all these systems can be assumed to be the same, we conclude that the features in ρ^t arise as a result of the electrostatic correlations between ions which are neglected in a typical mean field theory. We do, however, expect that in the case of systems under the influence of external electric fields of high strength, these variations in the density will be overpowered by the external bias and in such situations, Poisson-Boltzmann theory results will yield more accurate predictions of the total charge density. Some examples of modified Poisson-Boltzmann theories, such as by dos Santos and Levin,^{21,59} actually estimate the excess chemical potentials of the ions and incorporate those self-consistently in the Boltzmann distribution. These theories actually distinguish features caused by electrostatic correlations between the ions and would capture the features in Fig. 13.

C. Predictive potential and outlook

Our MD simulations and AHNC did not use any adjustable parameters and should in principle yield numerically exact results for the primitive model, which is corroborated by the excellent agreement. The AHNC has the advantage of being numerically efficient and converges generally within a few minutes on a single CPU. The algorithm, however, relies on many coupled numerical procedures, and the numerical parameters need to be chosen carefully to guarantee convergence, such that algorithm development is relatively involved (compared to, e.g., PB theory). The AHNC also yields the thermodynamic potentials on the fly, which are expensive to calculate with the CPMD, as well as the anisotropic correlation functions and potentials of mean force, which allow us to identify and separate the underlying mechanisms that are responsible for the observed features in the density profiles (as in Figs. 11 and 12). The AHNC does however rest on an approximation for the closure of the Ornstein-Zernike equation, the so-called Hyper-Netted Chain or HNC, which could lead to deviations that are likely to be *nil* for the chosen parameters. In the case of polarized interface systems, the accuracy on the density profiles is determined by the interfacial grid spacing, both for the simulations and the AHNC (lower grid spacing implies finer resolution of the interface and leads to higher accuracy). In some cases, the assumption of planar shapes for the dielectric interfaces may break down and curvature effects may become strong. We note that our CPMD simulations are well suited for systems with curved interfaces as demonstrated in Ref. 17 where ion distributions near a spherical interface were computed. More complex shapes will benefit from clever ways of meshing the interface but the overall CPMD procedure is similar to the method presented here for the two planar interfaces. Furthermore, the costs associated with the CPMD simulations of ions near interfaces of complex geometry would be similar to the costs incurred in the simulations for planar interfaces because the CPU time primarily depends on the interface area rather than its shape. We realize that, although our methods are numerically accurate for the primitive model, the model system itself assumes a homogeneous structureless medium without impurities and will not describe certain effects common in aqueous electrolytes.⁶⁰ The model system also assumes infinitely sharp dielectric boundaries, which may oversimplify the molecular width of, e.g., liquid-liquid or liquid-gas interfaces.¹⁹ However, the CPMD and AHNC could offer pathways to quantify those additional effects and derive effective potentials given that the ion thermodynamics within the model system is correctly treated. In the end, we note that our simulations and theory are versatile enough to treat the case of other multivalent salts (2:2, 3:3), asymmetric ion sizes, mixture of electrolytes, and the dynamical evolution of the soft ionic structure.

V. CONCLUSION

We calculate the non-monotonic density profiles of primitive model electrolytes in a dielectric confinement, with standard molecular dynamics and Car-Parrinello molecular

dynamics simulations and a theoretical method known as the AHNC. Both methods are free of adjustable parameters and show excellent agreement. We observe several features in the density profiles, such as adsorption at the ionic length scale, depletion over the electrostatic correlation length, and density oscillations over the entire profile, and connect a rich phenomenology of effects to three simple microscopic mechanisms. Two of these mechanisms result purely from ionic correlations and symmetry breaking at the interface and are missed entirely in mean field theories (by assumption). We show here that polarization charge at the confining boundaries can modify the ionic profiles significantly, although it appears to generate a smaller force on the ions compared to the thermal forces culminating from steric and electrostatic interactions between the ions, i.e., the ionic correlations, roughly above 0.1M concentrations. These mechanisms can induce charge segregation in asymmetric electrolytes that can increase, decrease, or reverse the effective charge of the boundary and can induce non-monotonic forces between the boundaries.^{6,7} Although we postpone the discussion of these forces to future work,⁶¹ we reduced the origin to three mechanisms that span the range of possible interfacial phenomena in the primitive model of electrolytes. The results of the CPMD and AHNC shed light on the origin of ion-specific and dielectric effects in confinement, which can be meaningful in the interpretation of effective interactions between nanoparticles, biomolecules, and membranes, and for the evaluation of interfacial activity in separation and process technologies.

ACKNOWLEDGMENTS

V.J. and Y.J. thank the support of the Office of the Director of Defense Research and Engineering (DDR&E) and the Air Force Office of Scientific Research (AFOSR) under Award No. FA9550-10-1-0167. J.W.Z. was funded by the NSF Grant No. DMR-1309027.

APPENDIX: ENERGY FUNCTIONAL EMPLOYED IN THE CPMD SIMULATION

Our CPMD simulation scheme is based on the variational functional shown in Eq. (1) and rewritten below,

$$I[\omega] = \frac{1}{2} \iint \rho_{\mathbf{r}} G_{\mathbf{r},\mathbf{r}'} (\rho_{\mathbf{r}'} + \Omega_{\mathbf{r}'}[\omega]) d\mathbf{r}' d\mathbf{r} - \frac{1}{2} \iint \Omega_{\mathbf{r}}[\omega] G_{\mathbf{r},\mathbf{r}'} (\omega_{\mathbf{r}'} - \Omega_{\mathbf{r}'}[\omega]) d\mathbf{r}' d\mathbf{r}. \quad (\text{A1})$$

Here, ρ and ω are the free and induced charge densities, respectively. As noted earlier, $G(\mathbf{r}, \mathbf{r}')$ is the Green's function given by

$$G(\mathbf{r}, \mathbf{r}') = |\mathbf{r} - \mathbf{r}'|^{-1} \quad (\text{A2})$$

and Ω is

$$\Omega_{\mathbf{r}}[\omega] = \nabla \cdot \left(\chi_{\mathbf{r}} \nabla \int G_{\mathbf{r},\mathbf{r}'} (\rho_{\mathbf{r}'} + \omega_{\mathbf{r}'}) d\mathbf{r}' \right), \quad (\text{A3})$$

where $\chi(\mathbf{r}) = (\epsilon(\mathbf{r}) - 1)/4\pi$ is the dielectric susceptibility and $\epsilon(\mathbf{r})$ is the permittivity at position \mathbf{r} which in general is spatially dependent.

In this appendix, we show the form of the above functional for the particular case of piecewise-uniform dielectric media with two (open) dielectric interfaces denoted as interfaces I and II. Interface I separates the dielectric region \mathcal{R}_1 with permittivity ϵ_1 from the region \mathcal{R}_2 with permittivity ϵ_2 . Interface II separates \mathcal{R}_2 from the region \mathcal{R}_3 characterized by permittivity ϵ_3 . In other words, the dielectric profile is given by

$$\begin{aligned}\epsilon(\mathbf{r}) &= \epsilon_1 & \mathbf{r} \in \mathcal{R}_1 \\ &= \epsilon_2 & \mathbf{r} \in \mathcal{R}_2 \\ &= \epsilon_3 & \mathbf{r} \in \mathcal{R}_3.\end{aligned}\quad (\text{A4})$$

The case of planar interfaces, which we analyze in our simulations, then becomes a special case of the functional derived below for the above dielectric profile. We first introduce some notations. We define ϵ_{mI} , ϵ_{mII} , ϵ_{dI} , and ϵ_{dII} as

$$\begin{aligned}\epsilon_{mI} &= \frac{\epsilon_1 + \epsilon_2}{2}, \quad \epsilon_{mII} = \frac{\epsilon_3 + \epsilon_2}{2}, \\ \epsilon_{dI} &= \frac{\epsilon_2 - \epsilon_1}{4\pi}, \quad \epsilon_{dII} = \frac{\epsilon_2 - \epsilon_3}{4\pi}.\end{aligned}\quad (\text{A5})$$

ϵ_m represents the mean of the dielectric permittivities on either sides of an interface and ϵ_d stores the amount of dielectric contrast at the interface. We denote $\hat{n}_i(\mathbf{s}_i)$ as the normal vector at \mathbf{s}_i where \mathbf{s} denotes the position vector of a point on the interface i . We will use indices i and j to identify an interface. On interface I, the normal vector is chosen to point from \mathcal{R}_1 to \mathcal{R}_2 and on the interface II, it is taken to point from \mathcal{R}_3 to \mathcal{R}_2 . In the particular case of dielectric configuration with planar interfaces that we analyzed in this paper, we have

\mathcal{R}_1 : $z \leq -H/2$, \mathcal{R}_2 : $-H/2 \leq z \leq H/2$, and \mathcal{R}_3 : $z \geq H/2$ with $z = -H/2$ plane as interface I and $z = H/2$ plane as interface II. As per our conventions, \hat{n}_I points in $(0,0,1)$ direction and \hat{n}_{II} points in $(0,0,-1)$ direction.

It is useful to introduce two functions \bar{G} and $\bar{\bar{G}}$ which we can be called indirect or renormalized Green's functions and are essentially interaction potentials between a pair of position coordinates. \bar{G}_i is defined as

$$\bar{G}_i(\mathbf{a}, \mathbf{b}) = \int G(\mathbf{a}, \mathbf{s}_i) \hat{n}_i(\mathbf{s}_i) \cdot \nabla_{\mathbf{s}_i} G(\mathbf{s}_i, \mathbf{b}) d\mathbf{s}_i \quad (\text{A6})$$

and $\bar{\bar{G}}_{ij}$ is given by

$$\begin{aligned}\bar{\bar{G}}_{ij}(\mathbf{a}, \mathbf{b}) &= \iint \hat{n}_i(\mathbf{s}_i) \cdot \nabla_{\mathbf{s}_i} G(\mathbf{a}, \mathbf{s}_i) G(\mathbf{s}_i, \mathbf{s}_j) \\ &\quad \times \hat{n}_j(\mathbf{s}_j) \cdot \nabla_{\mathbf{s}_j} G(\mathbf{s}_j, \mathbf{b}) d\mathbf{s}_i d\mathbf{s}_j.\end{aligned}\quad (\text{A7})$$

In the event of two interfaces (I and II), we have the following possibilities for these functions: \bar{G}_I , \bar{G}_{II} , $\bar{\bar{G}}_{I,I}$, $\bar{\bar{G}}_{II,II}$, $\bar{\bar{G}}_{I,II}$, and $\bar{\bar{G}}_{II,I}$.

Note that unlike G , \bar{G}_i and $\bar{\bar{G}}_{ij}$ are not symmetric, that is, $\bar{G}_i(\mathbf{a}, \mathbf{b}) \neq \bar{G}_i(\mathbf{b}, \mathbf{a})$ and $\bar{\bar{G}}_{ij}(\mathbf{a}, \mathbf{b}) \neq \bar{\bar{G}}_{ij}(\mathbf{b}, \mathbf{a})$. Also, $\bar{\bar{G}}_{ij}(\mathbf{a}, \mathbf{b}) \neq \bar{\bar{G}}_{ji}(\mathbf{a}, \mathbf{b})$ for $i \neq j$. In Eq. (A7), the self-interaction contributions (when $\mathbf{s}_i = \mathbf{s}_j$) coming from induced charges belonging to the same interface and same location (grid point) are approximated by a suitable analytical integral.²⁴

Using the dielectric profile of Eq. (A4) and the definitions of G and Ω from Eqs. (A2) and (A3) in Eq. (A1), we can reduce $I[\omega]$ to a form that can be written as

$$\begin{aligned}I[\omega] &= \frac{1}{2} \iint \rho(\mathbf{r}) R_{\rho\rho}(\mathbf{r}, \mathbf{r}') \rho(\mathbf{r}') d\mathbf{r} d\mathbf{r}' + \frac{1}{2} \iint \rho(\mathbf{r}) R_{\rho\omega_I}(\mathbf{r}, \mathbf{s}) \omega(\mathbf{s}) d\mathbf{r} d\mathbf{s} + \frac{1}{2} \iint \rho(\mathbf{r}) R_{\rho\omega_{II}}(\mathbf{r}, \mathbf{t}) \omega(\mathbf{t}) d\mathbf{r} d\mathbf{t} \\ &\quad + \frac{1}{2} \iint \omega(\mathbf{s}) R_{\omega_I\omega_I}(\mathbf{s}, \mathbf{s}') \omega(\mathbf{s}') d\mathbf{s} d\mathbf{s}' + \frac{1}{2} \iint \omega(\mathbf{t}) R_{\omega_{II}\omega_{II}}(\mathbf{t}, \mathbf{t}') \omega(\mathbf{t}') d\mathbf{t} d\mathbf{t}' + \frac{1}{2} \iint \omega(\mathbf{s}) R_{\omega_I\omega_{II}}(\mathbf{s}, \mathbf{t}) \omega(\mathbf{t}) d\mathbf{s} d\mathbf{t},\end{aligned}\quad (\text{A8})$$

where ω now denotes the surface charge density and \mathbf{s} , \mathbf{t} are position vectors associated with interfaces I and II, respectively. Minimizing this functional gives the correct ω on the two interfaces. Below, we describe the various R functions appearing in Eq. (A8).

The R functions characterize the effective interaction potential between two charges in different locations. The subscripts in the notation of these functions indicate the location of the charge and also whether it is a free charge or an induced charge. $R_{\rho\rho}$ denotes the effective potential between two free charges and is given by

$$\begin{aligned}R_{\rho\rho}(\mathbf{r}, \mathbf{r}') &= \frac{1}{\epsilon_r} G(\mathbf{r}, \mathbf{r}') + \frac{\epsilon_{dI}}{\epsilon_r \epsilon_{r'}} \bar{G}_I(\mathbf{r}, \mathbf{r}') + \frac{\epsilon_{dII}}{\epsilon_r \epsilon_{r'}} \bar{G}_{II}(\mathbf{r}, \mathbf{r}') \\ &\quad + \frac{\epsilon_{dI}^2}{\epsilon_r \epsilon_{r'}} \bar{\bar{G}}_{I,I}(\mathbf{r}, \mathbf{r}') + \frac{\epsilon_{dII}^2}{\epsilon_r \epsilon_{r'}} \bar{\bar{G}}_{II,II}(\mathbf{r}, \mathbf{r}') \\ &\quad + \frac{\epsilon_{dI} \epsilon_{dII}}{\epsilon_r \epsilon_{r'}} \bar{\bar{G}}_{I,II}(\mathbf{r}, \mathbf{r}') + \frac{\epsilon_{dI} \epsilon_{dII}}{\epsilon_r \epsilon_{r'}} \bar{\bar{G}}_{II,I}(\mathbf{r}, \mathbf{r}').\end{aligned}\quad (\text{A9})$$

The first term on the right-hand side of the above equation contains the Green's pair interaction potential. In the

evaluation of this term and the associated contribution to the total integral $I[\omega]$ of Eq. (A8), we assume $\mathbf{r} \neq \mathbf{r}'$. The next two terms involve the first renormalized Green's function \bar{G} and the final four terms comprise interactions of the form of $\bar{\bar{G}}$. Note that for the computation of the terms involving \bar{G} and $\bar{\bar{G}}$, we take into account the self-terms ($\mathbf{r} = \mathbf{r}'$) as these are well defined. $R_{\rho\omega_I}$ denotes the effective potential between a free charge and the induced charge on interface I and is given as

$$\begin{aligned}R_{\rho\omega_I}(\mathbf{r}, \mathbf{s}) &= \frac{\epsilon_r - \epsilon_{mI}}{\epsilon_r} G(\mathbf{r}, \mathbf{s}) + \frac{\epsilon_{dI}}{\epsilon_r} \bar{G}_I(\mathbf{r}, \mathbf{s}) + \frac{\epsilon_{dII}}{\epsilon_r} \bar{G}_{II}(\mathbf{r}, \mathbf{s}) \\ &\quad - \frac{\epsilon_{dI}(2\epsilon_{mI} - 1)}{\epsilon_r} \bar{G}_I(\mathbf{s}, \mathbf{r}) - \frac{\epsilon_{dII}(2\epsilon_{mI} - 1)}{\epsilon_r} \bar{G}_{II}(\mathbf{s}, \mathbf{r}) \\ &\quad + \frac{2\epsilon_{dI}^2}{\epsilon_r} \bar{\bar{G}}_{I,I}(\mathbf{r}, \mathbf{s}) + \frac{2\epsilon_{dII}^2}{\epsilon_r} \bar{\bar{G}}_{II,II}(\mathbf{r}, \mathbf{s}) \\ &\quad + \frac{2\epsilon_{dI} \epsilon_{dII}}{\epsilon_r} \bar{\bar{G}}_{I,II}(\mathbf{r}, \mathbf{s}) + \frac{2\epsilon_{dI} \epsilon_{dII}}{\epsilon_r} \bar{\bar{G}}_{II,I}(\mathbf{r}, \mathbf{s}).\end{aligned}\quad (\text{A10})$$

Similarly, $R_{p\omega_{II}}$ denotes the effective potential between a free charge and the induced charge on interface II and can be obtained from Eq. (A10) by swapping I with II and replacing \mathbf{s} with \mathbf{t} .

Next, we provide the expressions for the functions that represent the effective interactions between the induced charges on the interfaces. The effective interaction potential between two induced charges on interface I, $R_{\omega_I\omega_I}$, is given by

$$R_{\omega_I\omega_I}(\mathbf{s}, \mathbf{s}') = \epsilon_{m_I}(\epsilon_{m_I} - 1)G(\mathbf{s}, \mathbf{s}') + \epsilon_{d_I}(1 - 2\epsilon_{m_I})\bar{G}_I(\mathbf{s}, \mathbf{s}') \\ + \epsilon_{d_{II}}(1 - 2\epsilon_{m_I})\bar{G}_{II}(\mathbf{s}, \mathbf{s}') + \epsilon_{d_I}^2\bar{\bar{G}}_{I,I}(\mathbf{s}, \mathbf{s}') \\ + \epsilon_{d_{II}}^2\bar{\bar{G}}_{II,II}(\mathbf{s}, \mathbf{s}') + 2\epsilon_{d_I}\epsilon_{d_{II}}\bar{\bar{G}}_{I,II}(\mathbf{s}, \mathbf{s}'). \quad (\text{A11})$$

The evaluation of self-interaction ($\mathbf{s} = \mathbf{s}'$) terms is, as noted earlier, carried out via an analytically computed approximate form. Swapping I and II, and replacing \mathbf{s}, \mathbf{s}' with \mathbf{t}, \mathbf{t}' in Eq. (A11) leads to the expression for $R_{\omega_{II}\omega_{II}}(\mathbf{t}, \mathbf{t}')$. The last term on the right-hand side of Eq. (A8) involves the effective potential $R_{\omega_I\omega_{II}}$ which represents the interaction between an induced charge on interface I and an induced charge on interface II. $R_{\omega_I\omega_{II}}$ is given as

$$R_{\omega_I\omega_{II}}(\mathbf{s}, \mathbf{t}) = \epsilon_{m_I}(\epsilon_{m_{II}} - 1)G(\mathbf{s}, \mathbf{t}) + \epsilon_{m_{II}}(\epsilon_{m_I} - 1)G(\mathbf{t}, \mathbf{s}) \\ + \epsilon_{d_I}(1 - 2\epsilon_{m_I})\bar{G}_I(\mathbf{s}, \mathbf{t}) + \epsilon_{d_{II}}(1 - 2\epsilon_{m_I})\bar{G}_{II}(\mathbf{s}, \mathbf{t}) \\ + \epsilon_{d_I}(1 - 2\epsilon_{m_{II}})\bar{G}_I(\mathbf{t}, \mathbf{s}) + \epsilon_{d_{II}}(1 - 2\epsilon_{m_{II}})\bar{G}_{II}(\mathbf{t}, \mathbf{s}) \\ + 2\epsilon_{d_I}^2\bar{\bar{G}}_{I,I}(\mathbf{s}, \mathbf{t}) + 2\epsilon_{d_{II}}^2\bar{\bar{G}}_{II,II}(\mathbf{s}, \mathbf{t}) \\ + 2\epsilon_{d_I}\epsilon_{d_{II}}\bar{\bar{G}}_{I,II}(\mathbf{s}, \mathbf{t}) + 2\epsilon_{d_I}\epsilon_{d_{II}}\bar{\bar{G}}_{I,II}(\mathbf{t}, \mathbf{s}). \quad (\text{A12})$$

¹B. Honig and A. Nicholls, *Science* **268**, 1144 (1995).

²Y. Levin, *Phys. A: Stat. Mech. Its Appl.* **352**, 43 (2005).

³D. E. Clapham, *Cell* **131**, 1047 (2007).

⁴B. Eisenberg, *Faraday Discuss.* **160**, 279 (2013).

⁵J.-P. Hansen and H. Lowen, preprint [arXiv:cond-mat/0002295](https://arxiv.org/abs/cond-mat/0002295) (2000).

⁶L. Guldbrand, B. Jönsson, H. Wennerström, and P. Linse, *J. Chem. Phys.* **80**, 2221 (1984).

⁷P. Linse and V. Lobaskin, *Phys. Rev. Lett.* **83**, 4208 (1999).

⁸Z. Suo, *MRS Bull.* **37**, 218 (2012).

⁹F. J. Solis, G. Vernizzi, and M. Olvera de la Cruz, *Soft Matter* **7**, 1456 (2011).

¹⁰R. H. French, V. A. Parsegian, R. Podgornik, R. F. Rajter, A. Jagota, J. Luo, D. Asthagiri, M. K. Chaudhury, Y.-m. Chiang, S. Granick *et al.*, *Rev. Mod. Phys.* **82**, 1887 (2010).

¹¹G. Feng, R. Qiao, J. Huang, B. G. Sumpter, and V. Meunier, *ACS Nano* **4**, 2382 (2010).

¹²H. D. Abrua, Y. Kiya, and J. C. Henderson, *Phys. Today* **61**(12), 43 (2008).

¹³T. Vander Hoogerstraete, S. Wellens, K. Verachtert, and K. Binnemans, *Green Chem.* **15**, 919 (2013).

¹⁴M. Kandu, A. Naji, J. Forsman, and R. Podgornik, *J. Chem. Phys.* **137**, 174704 (2012).

¹⁵Z.-G. Wang, *J. Theor. Comput. Chem.* **07**, 397 (2008).

¹⁶M. Bier, J. Zwanikken, and R. van Roij, *Phys. Rev. Lett.* **101**, 046104 (2008).

¹⁷V. Jadhao, F. J. Solis, and M. Olvera de la Cruz, *Phys. Rev. Lett.* **109**, 223905 (2012).

¹⁸J. W. Zwanikken and M. Olvera de la Cruz, *Proc. Natl. Acad. Sci. U. S. A.* **110**, 5301 (2013).

¹⁹G. Luo, S. Malkova, J. Yoon, D. G. Schultz, B. Lin, M. Meron, I. Benjamin, P. Vasek, and M. L. Schlossman, *Science* **311**, 216 (2006).

²⁰J. R. Miller and P. Simon, *Science* **321**, 651 (2008).

²¹A. P. dos Santos and Y. Levin, *J. Chem. Phys.* **142**, 194104 (2015).

²²R. Wang and Z.-G. Wang, *J. Chem. Phys.* **139**, 124702 (2013).

²³Y. Nakayama and D. Andelman, *J. Chem. Phys.* **142**, 044706 (2015).

²⁴R. Allen, J.-P. Hansen, and S. Melchionna, *Phys. Chem. Chem. Phys.* **3**, 4177 (2001).

²⁵J. Rottler and A. C. Maggs, *Phys. Rev. Lett.* **93**, 170201 (2004).

²⁶D. Boda, D. Gillespie, W. Nonner, D. Henderson, and B. Eisenberg, *Phys. Rev. E* **69**, 046702 (2004).

²⁷V. Jadhao, F. J. Solis, and M. Olvera de la Cruz, *J. Chem. Phys.* **138**, 054119 (2013).

²⁸A. P. dos Santos, A. Bakhshandeh, and Y. Levin, *J. Chem. Phys.* **135**, 044124 (2011).

²⁹Z. Gan, H. Wu, K. Barros, Z. Xu, and E. Luijten, *J. Comput. Phys.* **291**, 317 (2015).

³⁰R. Kjellander and S. Marčelja, *Chem. Phys. Lett.* **112**, 49 (1984).

³¹R. Kjellander and S. Marčelja, *J. Chem. Phys.* **82**, 2122 (1985).

³²K. Nygård, S. Sarman, and R. Kjellander, *J. Chem. Phys.* **139**, 164701 (2013).

³³M. Deng and G. Em Karniadakis, *J. Chem. Phys.* **141**, 094703 (2014).

³⁴R. A. Curtis and L. Lue, *Curr. Opin. Colloid Interface Sci.* **20**, 19 (2015).

³⁵M. Hatlo, R. Van Roij, and L. Lue, *EPL* **97**, 28010 (2012).

³⁶R. R. Netz and H. Orland, *Eur. Phys. J. E* **1**, 203 (2000).

³⁷R. Kjellander and S. Marčelja, *Chem. Phys. Lett.* **142**, 485 (1987).

³⁸E. Wernersson, R. Kjellander, and J. Lyklema, *J. Phys. Chem. C* **114**, 1849 (2010).

³⁹J. Lyklema, *Chem. Phys. Lett.* **467**, 217 (2009).

⁴⁰J. Lyklema, *Adv. Colloid Interface Sci.* **147**, 205 (2009).

⁴¹C. Labbez, B. Jonsson, M. Skarba, and M. Borkovec, *Langmuir* **25**, 7209 (2009).

⁴²R. Car and M. Parrinello, *Phys. Rev. Lett.* **55**, 2471 (1985).

⁴³A. Parsegian, *Nature* **221**, 844 (1969).

⁴⁴G. M. Torrie and J. P. Valleau, *J. Chem. Phys.* **73**, 5807 (1980).

⁴⁵D. Boda, K.-Y. Chan, and D. Henderson, *J. Chem. Phys.* **109**, 7362 (1998).

⁴⁶G. I. Guerrero-Garcia, Y. Jing, and M. Olvera de la Cruz, *Soft Matter* **9**, 6046 (2013).

⁴⁷J.-P. Ryckaert, G. Ciccotti, and H. J. Berendsen, *J. Comput. Phys.* **23**, 327 (1977).

⁴⁸J. Hansen, G. Torrie, and P. Vieillefosse, *Phys. Rev. A* **16**, 2153 (1977).

⁴⁹R. Kjellander, T. Åkesson, B. Jönsson, and S. Marčelja, *J. Chem. Phys.* **97**, 1424 (1992).

⁵⁰V. Bojan, F. Pesth, T. Schilling, and M. Oettel, *Phys. Rev. E* **79**, 061402 (2009).

⁵¹S. Lang, V. Bojan, M. Oettel, D. Hajnal, T. Fransch, and R. Schilling, *Phys. Rev. Lett.* **105**, 125701 (2010).

⁵²E. Verwey and K. Niessen, *London, Edinburgh Dublin Philos. Mag. J. Sci.* **28**, 435 (1939).

⁵³O. J. Lanning and P. A. Madden, *J. Phys. Chem. B* **108**, 11069 (2004).

⁵⁴A. A. Kornyshev, *J. Phys. Chem. B* **111**, 5545 (2007).

⁵⁵S. L. Carnie and G. M. Torrie, *Adv. Chem. Phys.* **56**, 141 (1984).

⁵⁶I. Borukhov, D. Andelman, and H. Orland, *Phys. Rev. Lett.* **79**, 435 (1997).

⁵⁷E. Wernersson and R. Kjellander, *J. Chem. Phys.* **129**, 144701 (2008).

⁵⁸G. M. Torrie, J. P. Valleau, and C. W. Outhwaite, *J. Chem. Phys.* **81**, 6296 (1984).

⁵⁹A. Bakhshandeh, A. P. dos Santos, and Y. Levin, *Phys. Rev. Lett.* **107**, 107801 (2011).

⁶⁰B. Ninham, *Adv. Colloid Interface Sci.* **83**, 1 (1999).

⁶¹J. W. Zwanikken, Y. Jing, V. Jadhao, and M. Olvera de la Cruz, "Structure and thermal forces in confined electrolytes resolved by theory and simulations" (unpublished).